Role of simulation in understanding biological systems

M.R. Kaazempur-Mofrad [a,b], M. Bathe [a], H. Karcher [a,b], H.F. Younis [a,b],
H.C. Seong [a,c], E.B. Shim [a,c], R.C. Chan [d], D.P. Hinton [d], A.G. Isasi [a,b],
A. Upadhyaya [a,b], M.J. Powers [b,e], L.G. Griffith [b,e], R.D. Kamm [a,b,*]

[a] Department of Mechanical Engineering, Massachusetts Institute of Technology, 77 Massachusetts Avenue,
Cambridge, MA 02139, USA
[b] Division of Biological Engineering, Massachusetts Institute of Technology, Cambridge, MA, USA
[c] Department of Mechanical Engineering, Kumoh National University of Technology, South Korea
[d] Department of Radiology, Harvard Medical School and Massachusetts General Hospital, Boston, MA 02114, USA
[e] Department of Chemical Engineering, Massachusetts Institute of Technology, Cambridge, MA, USA

Abstract

Recent advances in computer performance and affordability have accelerated their application to understanding biological phenomena. Computational models are now an integral part of biological and biomedical research. This paper presents a range of examples that illustrate the important role that computational simulation plays in research in the biological and biomedical sciences.
© 2003 Elsevier Science Ltd. All rights reserved.

Keywords: Finite element method; Simulation; Biomechanics; Biological systems

1. Introduction

In recent years advances in the biological and medical sciences have increasingly relied on modeling and simulation. Development of modern computers has paralleled the need for quantitative understanding of complex biological problems, and itself has accelerated the development in our understanding of the biological phenomena and their relationships in biological systems. Benefiting from the marriage of biological and computational/mathematical sciences, we are no longer required to make compromises between scientific accuracy and mathematical/phenomenological tractability. This is of particular importance in biology and medicine where processes are composed of various time and length scales whose intrinsically complex interactions are critical for the function of biological systems. The need for strong cooperation between 'quantitative biologists' and applied scientists and engineers has been evident. Modeling and simulation have provided a successful medium for such cooperation as they provide an essential step and a powerful tool in understanding a biological system and its behavior. Simulations can never replace experiments in proving a biological hypothesis, but they can help biological experimentalists by providing a deeper understanding of experimental results and in improving experimental design.

This paper provides a range of examples that show the extensive role of mathematical modeling and computational simulation in biological and biomedical sciences. The examples are selective rather than inclusive, to allow for more exposure within the limited pages allotted for this article—we have favored problems that are tackled using continuum mechanics simulation techniques, specifically finite element methods. We hope that the examples contained herein will prove useful in illustrating the critical place of computer simulation in biological research. Example 1, *simulation of human carotid artery fluid and wall mechanics based on in vivo*

---

* Corresponding author. Tel.: +1-617-253-5330; fax: +1-617-258-8559.
E-mail address: rdkamm@mit.edu (R.D. Kamm).

magnetic resonance images (MRI) of normal volunteers, presents a finite element analysis of wall and fluid mechanics in a human carotid bifurcation using reconstructed models based on in vivo magnetic resonance imaging geometries and ultrasound velocity measurements. Wall shear stress and oscillatory shear index (OSI) distributions, both physiologically relevant fluid dynamic factors, are correlated to commonly diseased sites of atherosclerosis. In Example 2, *unsteady flow in a 3D collapsible tube*, a computational model is presented of a 3D compliant tube using a fully coupled fluid–structure interaction (FSI) approach, solving the full Navier–Stokes equations for the fluid flow. Collapsible tubes conveying a flow occur in a number of physiological applications, such as the pulmonary circulation and airways, the urethra, and the vocal cords. In Example 3, *modeling neutrophil transit through pulmonary capillaries*, we move to smaller (micrometer) length scales to study the transit of neutrophils in the pulmonary microcirculation. Neutrophils are sequestered in the lungs because they are required to deform through capillaries due to their relatively large size. This study sheds light on the biomechanics of neutrophil sequestration in pulmonary capillaries. The next application, *simulation of single cell micromanipulation using magnetic beads*, presents a finite element model for cell micromanipulation by magnetocytometry. The model serves as a robust tool for the analysis of detailed stress and strain fields induced in a cell monolayer, improving our understanding of the cell's mechanical properties and their variation under different mechanical and biological stimulations. Finally, in Example 5, *simulation of flow and transport in a microfabricated bioreactor for perfused 3D liver culture*, a model is developed of a 3D perfused bioreactor for liver tissue engineering. This system simulates in vivo perfusion conditions, most importantly shear stresses experienced by the liver cells, ensuring a physiologically relevant environment for hepatic tissue.

2. Examples

2.1. Simulation of human carotid artery fluid and wall mechanics based on in vivo MRI of normal volunteers

2.1.1. Introduction

The long standing hypothesis that fluid dynamic forces correlate with atherosclerotic disease has led to numerous analytical, numerical and experimental studies over the years [18,20]. Much of what inspired these studies is the observation that atherosclerotic disease is focal, typically occurring at sites of complex hemodynamics (blood flow dynamics) such as arterial bifurcations, junctions and/or regions of high curvature. Regions of low or oscillatory shear stress cause mono-

cyte (a particular type of white blood cell) adhesion to the endothelial wall, an early stage in atherogenesis. In addition to fluid shear stress, mechanical cyclic strain of the arterial wall may play a role in atherosclerosis. High values of cyclic strain have been implicated in the stimulation of endothelial and smooth muscle cells [22].

The primary goal of this study is thus to validate the hypothesis that low or oscillatory shear and/or high cyclic strain correlate with known sites of inflammation in the carotid bifurcation. This is carried out using solid and fluid (and coupled solid–fluid) 3D computational finite element method (FEM) analyses. Fluid boundary conditions are based on realistic flow profiles obtained using ultrasound measurements and arterial geometries are obtained from in vivo MRI, each of human volunteers and patients.

2.1.2. Modeling

Three normal (healthy) volunteers, referred to as NV1, NV2 and NV4 (ages 24–30) were chosen for this study. The procedure for the processing of each normal volunteer's data is composed of several stages: MRI, edge detection, lofting, flow profile generation and finally, finite element analysis. The edge detection protocol reads the geometry MRI data to generate a series of 2D slices. The 3D vascular structure is reconstructed using a solid modeling software, by lofting across the 2D cross-sectional structures of each level of the carotid bifurcation. The geometry, velocity at the inlet (common carotid), and velocity at the outlet (internal carotid) files (from ultrasound measurements) are then imported into the FEM software to simulate the in vivo fluid dynamics and wall mechanics. An overall schematic of this process is illustrated in Fig. 1.

The arterial wall is modeled as a non-linear, isotropic, hyperelastic material. The strain energy density function is given by [9]

$$W = \frac{a}{b}[e^{(b/2)(I_1-3)} - 1] \qquad (2.1)$$

where I_1 is the first invariant of the strain tensor and a and b ($a = 44.25$ kPa, $b = 16.73$) are material constants that reflect the arterial tissue composition. This exponential form is appropriate for arterial mechanics because it captures the strain-stiffening behavior of collagen. Blood is treated as an incompressible, Newtonian fluid (an assumption that has repeatedly been shown to be valid for large arteries—see, for example [4]) with viscosity 0.004 Pa s and density 1100 kg/m^3. The full Navier–Stokes equations and continuity are used to model the fluid assuming laminar flow and are fully coupled to the solid equations of motion.

2.1.3. Numerical methods

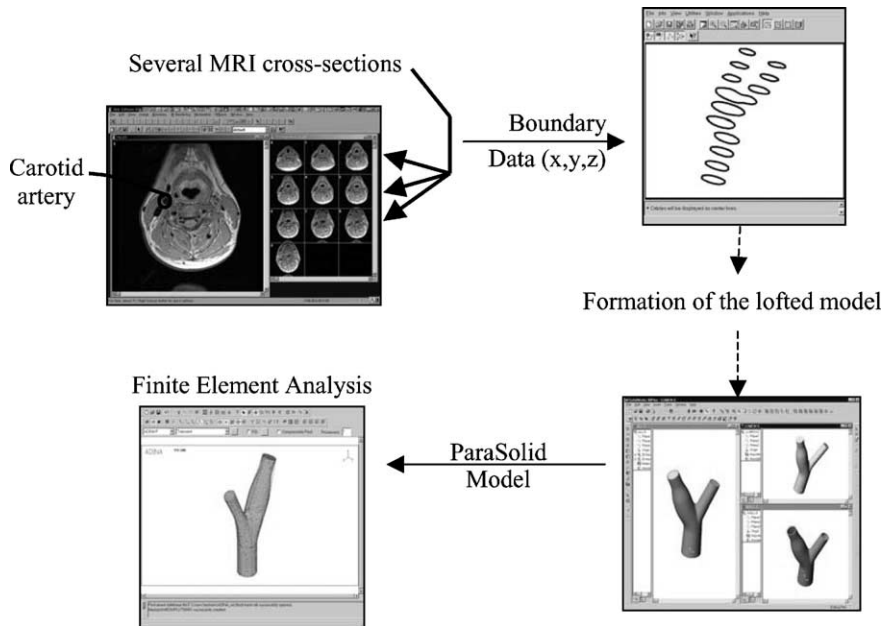A commercial finite element program is used to solve the fully coupled solid/fluid governing equations

Fig. 1. Procedure to be used to import MRI image data from source into finite element package. Note that both fluid and solid domains are generated.

(ADINA 7.4, Watertown, MA). Unstructured meshes are used due to the complexity of the geometries involved. The element size used for the solid and fluid domains is 0.4 mm (NV1 and NV4 solid simulations used a 0.45 mm mesh), which provides 2–3 solid elements through the wall thickness and 15–20 elements across the common carotid. Eleven-node quadratic elements are used for the wall domain, while 4-node linear elements are utilized for the fluid domain computations. The solid response is analyzed using the updated Lagrangian formulation, accounting for large displacements and strains [1], and the arbitrary Lagrangian Eulerian formulation is employed for the fluid equations of motion, necessitated by the moving fluid boundaries [3].

2.1.4. Results

The maximum pressure drop along a healthy carotid bifurcation (primarily due to inertial effects) is on the order of 700 Pa, or no more than ∼5% of the systolic pressure. This, in addition with the fact that the arterial wall behaves in a *pseudoelastic* manner [13], enabled us to perform a static inflation of the arterial wall models to gain insight into the strain levels within the bifurcation. An axial stretch of 10% was applied to the solid domain (the MRI-reconstructed models were first shrunk uniformly by 10% to simulate the ex-vivo load-free state; this compensated for the distensibility due to blood pressure as well as the axial pre-stretch) as measured in situ by Delfino [8]. The pressure was ramped incrementally from zero to diastolic pressure (80 mm Hg),

and then to systolic pressure (120 mm Hg). The solutions were stored only at systole and diastole and the Von Mises cyclic strain was computed as the difference between these two states.

2.1.5. Results: wall shear stress

All three normal volunteer models (Fig. 2) exhibit a large continuous region of low τ_w in the carotid bulb, where late atherosclerotic inflammation develops [18]. High τ_w is observed at the apex in all three cases: NV1, NV2 and NV4. The apex experiences τ_w values between 6 and 10 Pa and there exists a very small localized region of τ_w above 10 Pa, which seems to be closer to the inner wall of the external carotid in all three cases. Values of τ_w above 1.5 Pa induce endothelial quiescence (a stable, non-proliferative state) and a gene expression profile consistent with the absence of disease [20].

Another parameter investigated for each normal volunteer is the OSI as defined by Ku et al. [18]. The OSI is a dimensionless measure that quantifies the amount of time during a heartbeat that a particular wall region experiences cross or reverse flow. A common feature among all geometries (data not shown) is that the areas of high OSI lie within the areas of low τ_w; this confirms that these are also areas of flow reversal.

2.1.6. Results: cyclic strain

A common feature seen in all the cyclic strain bandplots at the interior face of the bifurcation (corresponding to strain experienced by the endothelium) (Fig. 3) is
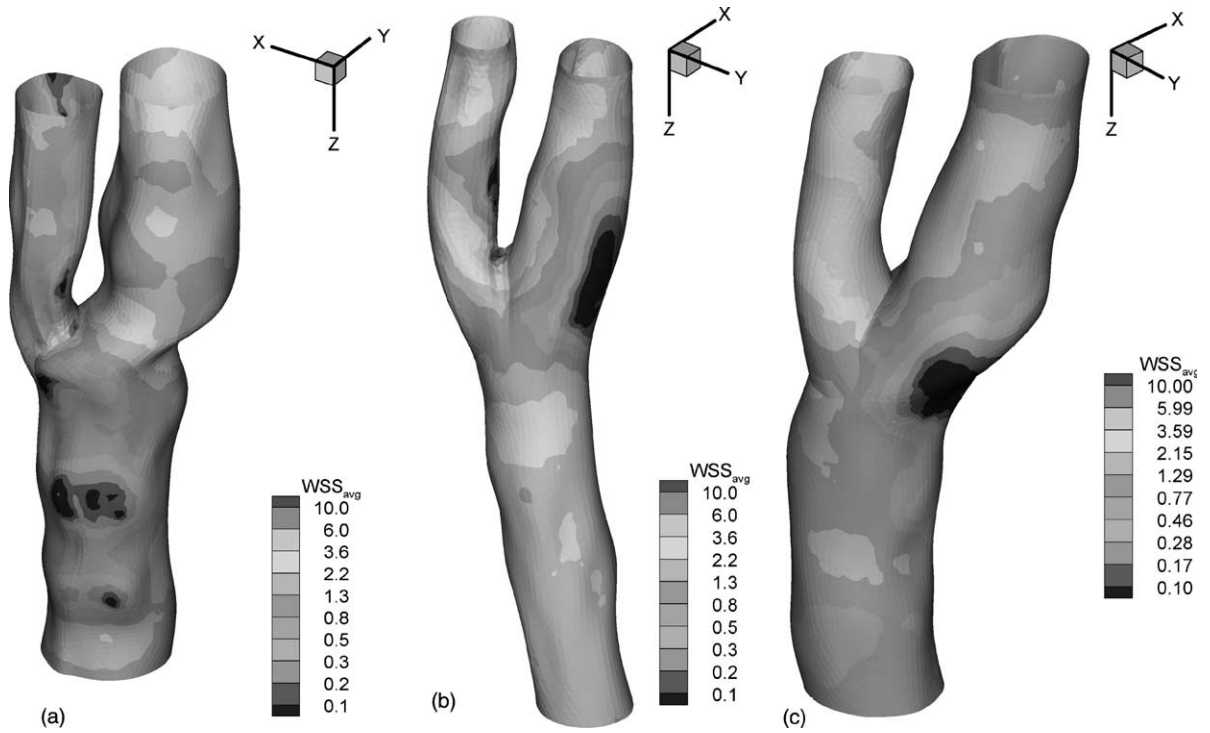
Fig. 2. Average wall shear stress (WSS$_{ave}$) plots (Pa) over the cycle for each NV. Logarithmic scales are used to emphasize low (<0.5 Pa) wall shear stress below which an atherosclerotic gene expression profile is expected. NV1 (a), NV2 (b), NV4 (c).
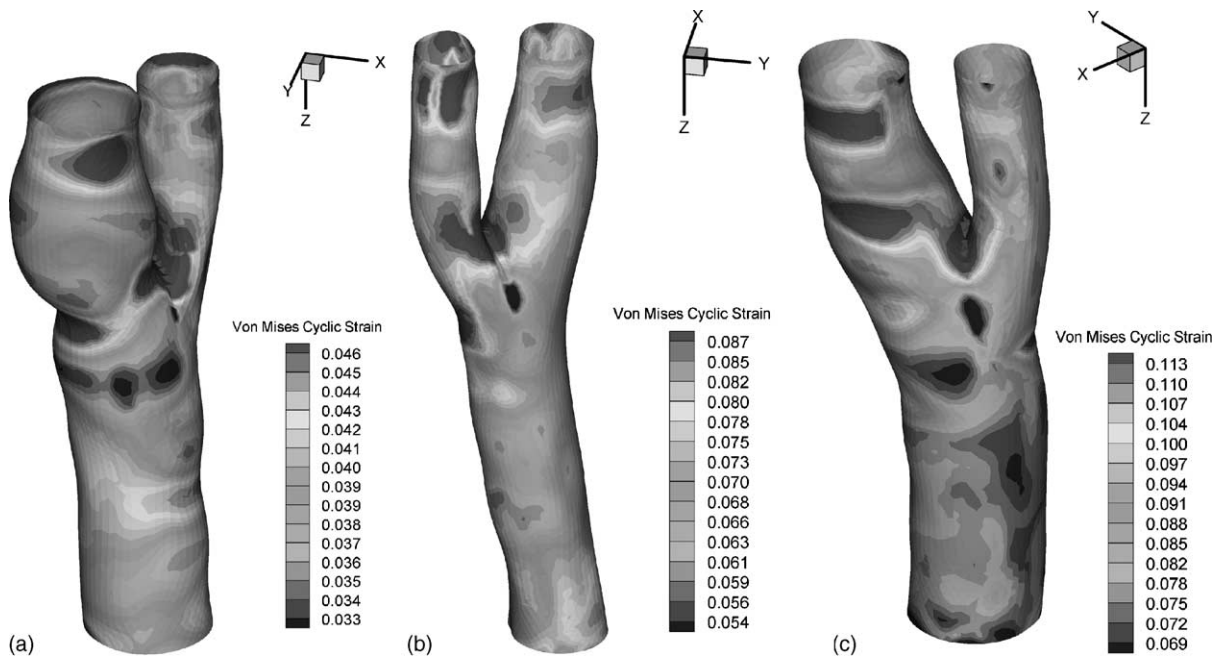

Fig. 3. Von Mises cyclic strain for each NV. Cyclic strain is computed as the difference between systolic and diastolic strains. NV1 (a), NV2 (b), NV4 (c).

that the levels of cyclic strain are highest at the apex (NV1: 14%; NV2: 11%; NV4: 6%). A second area of high cyclic strain in all the geometries, although of smaller magnitude, is at the external-common adjoining wall (NV1: 11%, NV2: 9%, NV4: 5%). These are both commonly observed sites of atherosclerosis.

2.1.7. Summary

Finite element models of arterial-blood flow mechanics are established based on in vivo MRI measurements of structural anatomy and ultrasound measurements of flow boundary conditions in healthy human carotid bifurcations. Localized separated flow regions are observed, especially near the outer wall of the internal carotid (the carotid bulb), in response to the localized abrupt changes in the curvature and cross-sectional area of the arterial wall. Localized high cyclic strains are observed at the flow divider and along the outside wall of the external carotid, both of which are common sites of early inflammation. These observations provide evidence that atherosclerosis cannot be attributed to a single mechanical factor and that development of the disease is a complex process involving multiple biomechanical pathways.

2.2. Unsteady flow in a 3D collapsible tube

2.2.1. Introduction

Most fluid carrying vessels in the body, e.g. veins, arteries, pulmonary vessels and airways, are elastic and may collapse when the transmural (inside–outside) pressure falls below a critical value. Previous studies of collapsible tubes can be categorized as follows: (i) Lumped-parameter or 1D flow models provided a basic understanding of the behavior of the collapsible segment using the *tube law*, an expression relating the transmural pressure to the local cross-sectional area (e.g. [11]). (ii) 2D flow models investigated steady and unsteady flows in collapsible channels by solving the Navier–Stokes equations (e.g. [19]). These models abandoned the use of the tube law and instead modeled the collapsible wall as

a thin elastic membrane having zero thickness. (iii) One published 3D model that examined the Stokes flow regime and used thin shell theory to approximate the collapsible wall [14].

The goal of the present study is to develop a realistic simulation of a 3D compliant tube using a fully coupled FSI approach, solving the full Navier–Stokes equations to analyze fluid flow in the tube. The wall is modeled as an elastic solid of finite thickness.

2.2.2. Modeling

We consider a short section of compliant tubing mounted between two rigid tubes (Fig. 4). To induce collapse, a small circumferential pressure perturbation is imposed on the wall. The inlet pressure is set to zero and the normal traction at the outlet surface is linearly decreased from 0 to −4 kPa in 0.8 s and then maintained for an additional 0.2 s. The fluid is assumed to be Newtonian and incompressible with dynamic viscosity $\mu_f = 0.01$ kg/m s and density, $\rho_f = 1000$ kg/m^3. The compliant wall has the properties of latex rubber (Young's modulus $E = 6.07$ MPa, density $\rho_s = 1000$ kg/m^3, and Poisson's ratio $v = 0.49$).

2.2.3. Numerical methods

The fully coupled governing equations are solved using a commercial finite element software program (ADINA, Watertown, MA). Linear tetrahedral elements are used for the fluid, while the solid wall region is discretized using 20-node hexahedral elements. The Arbitrary Lagrangian Eulerian formulation is employed for the fluid domain.

2.2.4. Results

The wall and fluid regions of the collapsed tube are shown in Figs. 5 and 6, respectively. As evident in the figures, the region of maximal collapse occurs near the downstream end, the wall deforming into a three-lobed configuration, consistent with the study of Heil [14]. During the transient reduction in downstream pressure, flow rate increased and reached a maximum value but
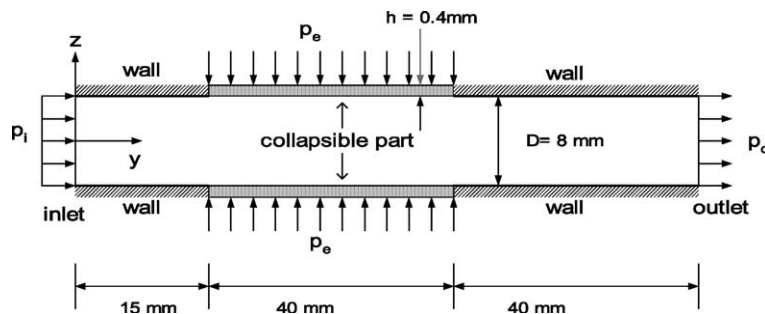

Fig. 4. 3D model for collapsible tube flow. Schematic of geometry and loading.
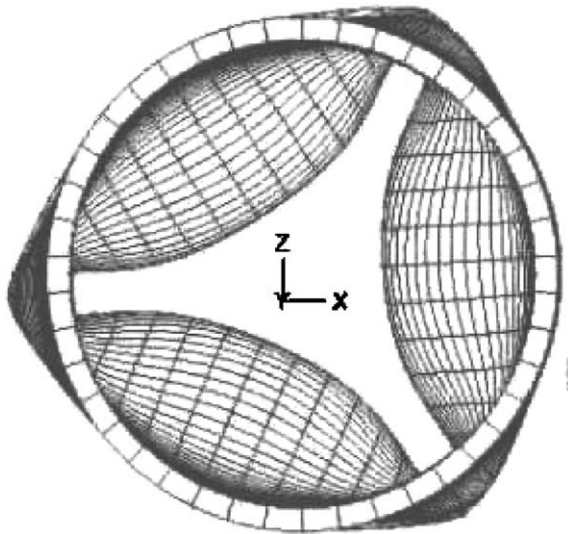
Fig. 5. Axial view of the deformed wall of the collapsible section in Fig. 4 showing the 3-lobed buckling pattern (downstream pressure = −4 kPa).
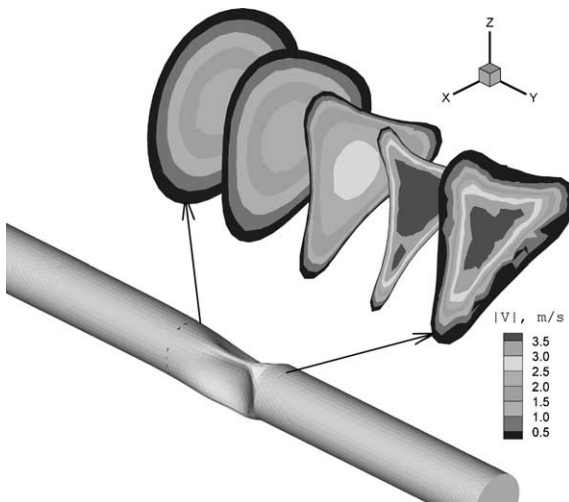

Fig. 6. Inner boundary of the collapsed wall. Cross-sections of the deformed region are demonstrated along with contourplots of flow velocity magnitude.

then abruptly fell, ultimately attaining a steady value at the lowest pressure of −4 kPa. Further calculations are needed to determine to what extent this system exhibits flow limitation as is typically observed experimentally.

2.2.5. Summary

A computational model is presented of a 3D compliant tube using a fully coupled FSI approach, solving the full Navier–Stokes equations for the fluid.

2.3. Modeling neutrophil transit through individual pulmonary capillaries

2.3.1. Introduction

Neutrophils are granulocytic white blood cells that are larger in mean diameter than approximately 40% of capillary segments in the human lungs [7,15]. Due to their high internal viscosity and the low driving pressures present in the pulmonary microcirculation, neutrophils require up to minutes to transit individual capillary segments, leading to their accumulation in the lungs. Moreover, stimulation with the chemoattractant fMLP (*N*-formyl-L-methionyl-L-leucyl-L-phenylalanine) has been shown to decrease their deformability due to actin reorganization and to increase their retention in the lungs [23].

The goal of this simulation is to quantify the effects of fMLP-stimulation on neutrophil mechanical properties and to determine the relative influences of capillary geometry and fMLP on neutrophil transit times through individual pulmonary capillaries. The results are used to gain insight into the biomechanics of neutrophil sequestration in the lungs.

2.3.2. Modeling: neutrophil

The neutrophil is modeled as a homogeneous, incompressible, viscoelastic Maxwell material bounded by constant surface tension, γ. The undeformed radius, the elastic shear modulus, and the viscosity of the cell are denoted R_{cell}, G_{cell}, and μ_{cell}, respectively. The model incorporates the elastic restoring effects of the actin-rich cortical layer lining the periphery of the cell, lying just below its external lipid bilayer, with the ability to capture both its elastic, solid-like short time-scale behavior as well as its viscous, fluid-like long time-scale behavior [10].

2.3.3. Modeling: indentation

Previously performed indentation experiments on passive and fMLP-stimulated neutrophils are simulated using finite element analysis to determine the effects of fMLP on neutrophil mechanical properties [23]. The cell is placed on a rigid, frictionless substrate and indented at a constant rate with a rigid indenter of smaller diameter than the cell. The shear modulus and viscosity (G_{cell}, μ_{cell}) of the cell are varied to best fit the experimental indentation data for three different concentrations of fMLP, corresponding to 0, 10^{-9} and 10^{-6} M.

2.3.4. Modeling: capillary flow

Individual pulmonary capillaries are modeled as axisymmetric and characterized by two geometric parameters: R_{min}, the minimum radius of the capillary constriction and a, the constant, in-plane radius of curvature of the constriction. The endothelial glycocalyx

is modeled as a rigid constant thickness layer that is highly permeable to the flow of plasma by placing a contact surface 100 nm from the capillary wall. Plasma is treated as an incompressible Newtonian fluid with the properties of water, and a constant physiological pressure drop, ΔP, between 20 and 80 Pa is applied across the ends of the capillary.

2.3.5. Numerical methods

The commercially available finite element program ADINA 7.5 (Watertown, MA) is used to solve the mathematical models presented above. The updated Lagrangian Hencky kinematic formulation is employed for the cellular domain and the constraint function method is used to satisfy the nonlinear contact conditions [1]. Axisymmetric 4/1 u/p solid elements are used to discretize the interior cellular domain and 2-node shell elements with an initial state of constant equibiaxial stress are used to model the cell's bounding surface tension. Plasma is spatially discretized with triangular 3-node fluid elements. Both the solid and fluid elements satisfy the inf–sup condition for stability and optimality in incompressible analysis [6]. The FSI capabilities of ADINA are used to solve the capillary flow problem, in which the solution obtained is fully coupled, in the sense that force equilibrium and displacement/velocity/acceleration continuity are satisfied at the neutrophil–plasma interface.

2.3.6. Results

The Maxwell model with surface tension was able to capture the experimental response of the neutrophil in indentation for the various levels of fMLP (Fig. 7). The effects of fMLP on neutrophil mechanical properties are
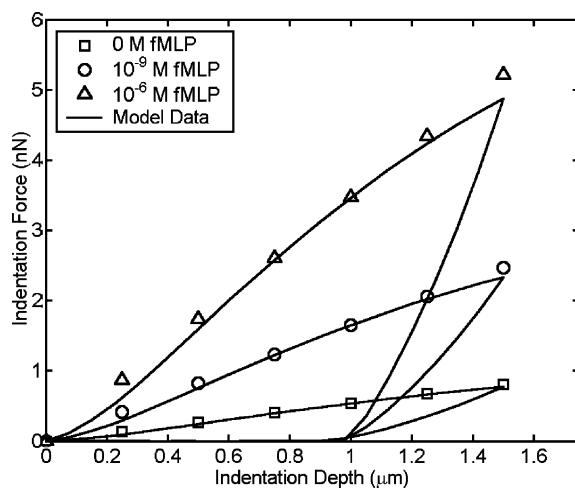
Fig. 7. Maxwell model fit to mean experimental indentation data for non-stimulated, 10^{-9} M, and 10^{-6} M fMLP-stimulated neutrophils incubated at room temperature. Symbols correspond to experimental data and lines to the models in Table 1.

Table 1
Non-stimulated and fMLP-stimulated neutrophil model parameters determined via indentation for the Maxwell model with constant surface tension ($\gamma = 31$ pN/m)

fMLP concentration (M)	Experimental indentation stiffness (nN/μm)	G_{cell} (Pa)	μ_{cell} (Pa·s)	γ (pN/μm)
0	0.540	185	30.8	31
10^{-9}	1.65	625	104	31
10^{-6}	3.48	1350	225	31

Indentation stiffness is defined as the slope of the linear force–displacement curve.

significant, increasing G_{cell} and μ_{cell} by more than threefold and sevenfold in the 10^{-9} and 10^{-6} M fMLP cases, respectively (Table 1).

The dimensionless transit time of the cell, $T^* = T\Delta P/\mu_{cell}$, where T denotes the dimensional transit time from entry to exit of the capillary constriction, may be expressed as a function of the relevant dimensionless groups in the capillary model as

$$T^* = f(G^*, R^*, a^*, \gamma^*) \tag{2.2}$$

where $G^* = G_{cell}/\Delta P$, $R^* = R_{min}/R_{cell}$, $a^* = a/R_{cell}$, and $\gamma^* = \gamma/(R_{min}\Delta P)$. Fixing γ^* in the physiologically relevant range of 0.26–0.31 and noting that T^* becomes independent of G^* in the viscous deformation dominated limit $G^* \gg 1$, the capillary flow results may be expressed as

$$T^* = 0.58(a^*)^{-0.50}[(R^*)^{-5.0} - 1] \tag{2.3}$$

for $0.50 \leqslant R^* \leqslant 0.75$ and $2 \leqslant a^* \leqslant 45$ (Fig. 8). In the case where G^* is not restricted to be $\gg 1$, a correction to the above expression is required to account for the effects of cellular elasticity, which tends to reduce the cell's transit time, most significantly as $R^* \to 1$ [2]. Fig. 9 shows a typical result obtained for the flow of the cell into a capillary constriction. The pressure concentration in the cell at the wall increases as the angle is decreased, tending to squeeze the cell at a faster rate, explaining the inverse dependence of T^* on a^* in Eq. (2.3).

2.3.7. Summary

We quantify the effects of the chemoattractant fMLP on neutrophil mechanical properties by simulating previously performed indentation experiments using finite element analysis (Table 1). In an independent study, we simulate neutrophil transit through narrow pulmonary capillary segments and derive a general dimensionless expression relating the cell's transit time, T^*, to capillary geometry, namely minimum capillary radius, R^*, and entrance radius of curvature, a^* (Eq. (2.3)). Results indicate that capillary entrance radius of curvature may be a significant determinant of neutrophil transit time, in
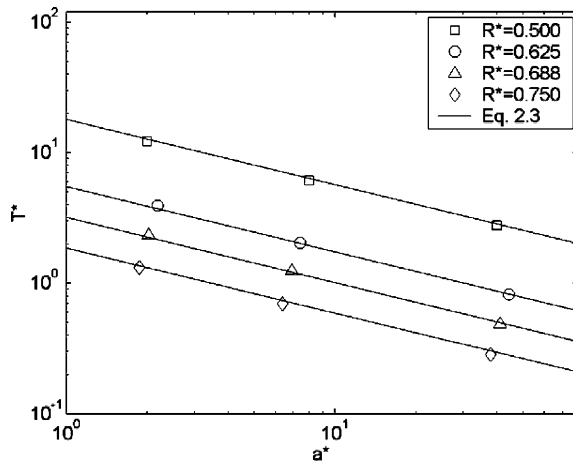
Fig. 8. Dependence of T^* on a^* for four values of R^* in the viscous deformation dominated limit $G_{\text{cell}} \gg \Delta P$.
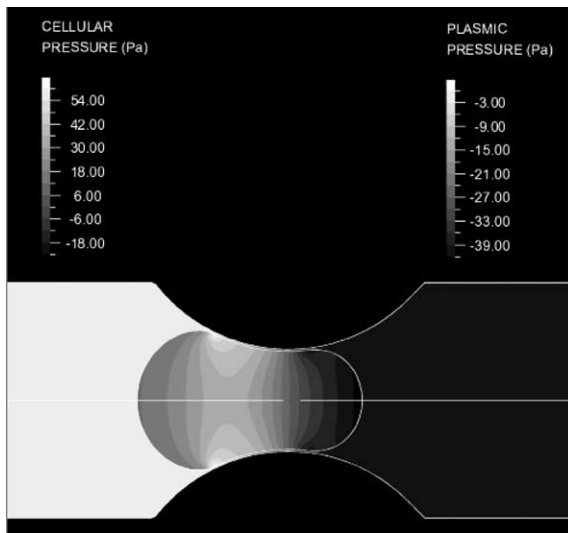

Fig. 9. Pressure band-plot of neutrophil entering a typical capillary constriction, illustrating the pressure concentration in the cell near the wall.

addition to minimum capillary radius and fMLP-stimulation level.

2.4. Simulation of single cell manipulation using magnetic beads

2.4.1. Introduction

In order to provide insight into the mechanical response of a cell during magnetocytometry experiments we simulate the application of a controlled force to a single cell via magnetic microbeads. A computational model is developed based on finite element methods to analyze the forcing of one microbead on a cell monolayer and determine the patterns of induced mechanical stress/strain. Detailed distributions of displacement and stress fields can then be used to: (i) determine the mechanical properties of the cells, (ii) correlate the localized stress/strain patterns to biological responses of the cell, and finally (iii) offer simple theoretical models of experimental observations.

2.4.2. Modeling

The model consists of two parts: a cell monolayer and a magnetic bead of diameter 4.5 μm. The cell monolayer is itself composed of (i) a cylindrical domain (10 μm high and 60 μm in diameter) accounting for the cytoskeleton and (ii) a 100 nm thin plate representing the membrane and the actin cortex. The model allows for increasing the contact surface between the bead and the membrane and for the variation of cell properties and dimensions. Table 2 summarizes the material properties currently used in the model. A zero-displacement boundary condition is imposed at the bottom surface, i.e. the cell monolayer is fixed to a rigid substrate. No constraint is imposed on the outer perimeter of the cell monolayer (zero stress traction boundary condition). Magnetic forcing on the bead is produced by a 1.7 μm horizontal displacement imposed at a rate of 1 μm/s on a horizontal diameter of the bead.

2.4.3. Numerical methods

The 3D model is solved using the commercially available finite element software program ADINA 7.5 (Watertown, MA). The cytoskeletal mesh consists of 25,632 quadrilateral elements with 25,541-nodes, while the thin membrane is modeled with a single layer of nodes and 1440 shell elements.

2.4.4. Results

The displacement field (see Figs. 10 and 11) exhibits a pulling/squeezing pattern characteristic of bead rolling. Interestingly, a zero-displacement zone is visible immediately beneath the bead. A cutoff radius around 10 μm is observed, in agreement with both theoretical estimations [5] and experimental measurements [16]. In all simulations, the maximum displacement inside the cytoskeleton in the direction of forcing is roughly half of that applied to the bead. This is qualitatively in agreement with membrane displacements of around 0.1 μm reported in [16]—quantitative comparisons are not possible as measurements are not available in the immediate vicinity of the bead.

Stresses are largely confined to the immediate vicinity of the bead and are dominated by shear rather than normal stresses. For example, at 1.5 μm bead displacement, the maximum effective stress is 220 Pa (see Fig. 12)

Table 2
Material properties used in the model

Part of the model	Material	Constants	References
Magnetic bead	Incompressible homogenous isotropic elastic (Hooke)	Young's modulus $E = 10,000$ Pa	*
Cell membrane and actin cortex	Incompressible homogenous isotropic viscoelastic (Maxwell)	Bending stiffness $D = 2 \times 10^{-19}$ N·m, Shear Viscosity $\mu' = 10^{-6}$ N·s/m	[12,17]
Cytoskeleton	Incompressible homogenous isotropic viscoelastic (Maxwell)	Shear modulus $G = 100$ Pa, viscosity $\mu = 100$ Pa·s	[24]

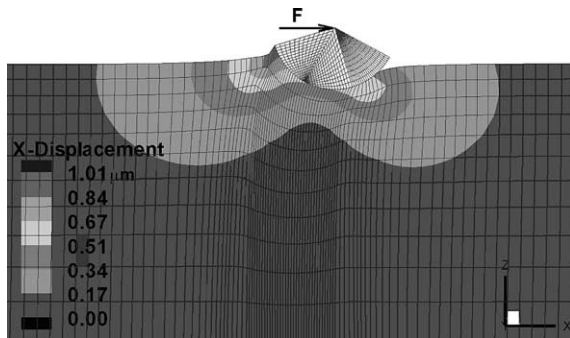*The material constants are chosen so that the magnetic bead is rigid.

Fig. 10. Cross-sectional view of a part of the 10 µm thick monolayer: displacement field in the x-direction after a 1.5 µm bead displacement. Only a part of the bead is displayed. The arrow represents the bead displacement. Displacements given in µm.

Fig. 11. Cross-sectional view of a part of the 10 µm thick monolayer: displacement field in the z-direction after a 1.5 µm displacement. Only a part of the bead is displayed. The arrow represents the bead displacement. Displacements given in µm.
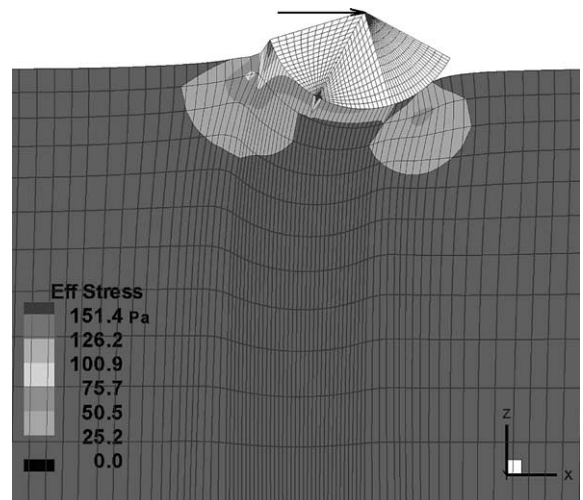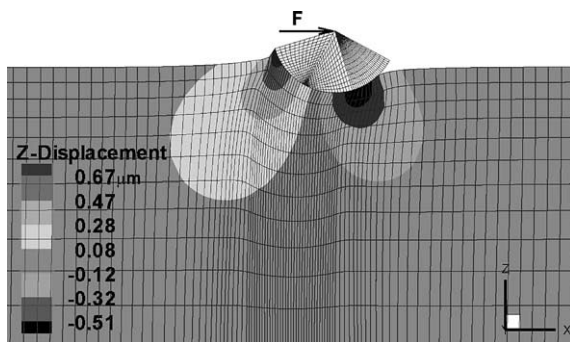

Fig. 12. Cross-sectional view of a part of the 10 µm thick monolayer: effective stress field in the x-direction after a 1.5 µm bead displacement. Stresses given in Pa.

Fig. 13. Bead reaction force versus bead displacement for two thicknesses of monolayer. The displacement is imposed at a rate of 1 µm/s. The inset shows the reaction of the bead when the displacement is imposed at a rate of 1 µm/s and then bead position is fixed at 1.5 µm for an additional 0.5 s.

whereas the extremum pressure is −115 Pa (data not shown).

Evident in Fig. 13 is the non-linear relationship between reaction force (i.e. the resisting force on the bead) and the imposed displacement of the bead; the slope decreases with increasing displacement. This is likely due to stress relaxation in the viscoelastic monolayer. In order to examine this hypothesis, we performed a
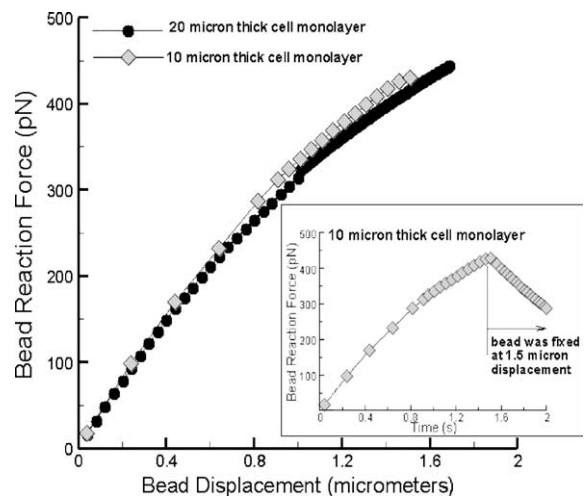
simulation in which the microbead was kept fixed after reaching the 1.5 μm displacement, and observed that the resisting reaction force on the cell fell from 430 to 290 pN within 0.5 s (see inset panel in Fig. 13). The shape of the curve was indeed characteristic of a viscoelastic response.

Using values in Table 2, we calculate the relaxation time scales: 1 s for the cytoskeleton and 1 μs for the membrane and actin cortex. Because the forcing time scale is comparable with the cytoskeleton relaxation time scale and more importantly because it greatly exceeds that of the membrane, we infer that the force–displacement curve is effectively dominated by the characteristics of the cytoskeleton.

Results for the 10 μm thick monolayer (typical of endothelial cells) and 20 μm thick monolayer (typical of epithelial cells) are remarkably similar, consistent with the observation that displacements are confined to a region extending just a few micrometers from the bead.

The overall character of the reaction–displacement curves compares favorably with measurements recently performed in our laboratory [16]: for beads displaced a distance of 1.5 μm at a rate of roughly 1 μm/s, the resulting reaction force is comparable to the predicted 450 pN.

2.4.5. Summary

A finite element model is developed for the study of a cell's response to mechanical stimulation. The model presents a robust tool for detailed examination of the strain/stress patterns induced in the cell monolayer. Results demonstrate that a simplified homogeneous, isotropic and continuum model for the cell can at least qualitatively mimic the cell's response patterns.

2.5. Simulation of flow and mass transport in a bioreactor for perfused 3D liver culture

Under standard in vitro cell culture conditions, hepatocytes rapidly lose their liver-specific metabolic and biosynthetic characteristics. This has led to development of a variety of cell culture techniques, none of which, however, yet replicates a comprehensive environment for the important functions of the liver. The overall goal of this work is to develop a 3D perfusion culture, providing a suitable scaffold for tissue morphogenesis and a homogeneous distribution of flow and mass transfer to meet the metabolic demands of the cells. Detailed analysis of the fluid flow and transport patterns in the reactor is required in order to ensure that the cells enjoy metabolically sufficient oxygenation and physiologically relevant shear stresses. An FEM model is developed to estimate the level of shear stress experienced by the cells under the influence of bulk flow at the surface of the chip and perfusion flow in the microchannels.

2.5.1. Reactor design

A cross-flow perfusion reactor that addresses these constraints was designed and fabricated [21]. At the heart of the reactor is the cell scaffold, comprised of a thin (<250 μm) silicon sheet permeated by a regular array of channels and seated atop a microporous filter and located between the upper and lower chambers of a flow-through housing. The functional unit of the bioreactor system is an individual channel, attempting to mimic a single capillary bed as the functional unit of liver. Current designs provide for repeated in situ observation of cells via light or two-photon microscopy during culture of the 3D perfused tissue structures. Further description of the design and the corresponding morphological behavior of primary hepatocytes maintained under perfusion is given in Powers et al. [21].

2.5.2. Modeling and numerical methods

The computational model involves a finite element solution of the full 3D Navier–Stokes equations using commercial software ADINA V. 7.4 (Watertown, MA). The Reynolds number, based on the width of the upper chamber and the diameter of the tissue flow-channels, respectively, is of order one in the interior of the upper chamber and of order 0.1 within the scaffold microchannels for finite cross-flow (see Fig. 14). Boundary conditions for the microchannel regions in the scaffold are set to reflect the extremes of either zero cross flow rate or experimental values of cross-flow with open channels.
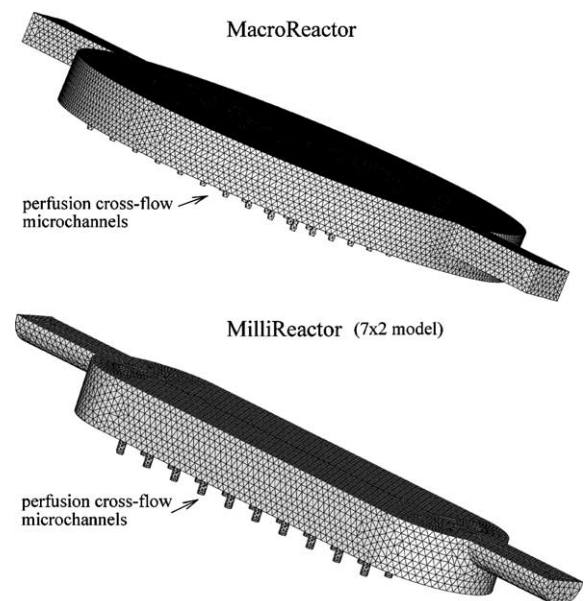

Fig. 14. A schematic of the computational geometry and mesh in the MacroReactor (top panel) and MilliReactor (bottom panel) models.

2.5.3. Results

Shear stress in the region near the center of the scaffold is approximately 0.01–0.02 Pa and that near the sidewalls of the reactor is about 0.005–0.01 Pa (see Fig. 15). Cells in channels closest to the inlet and outlet ports experience shear stresses of about 0.02–0.035 Pa, the maximum observed. Shear stress distributions at the chip surface for the extreme case where cells have completely plugged channels are not significantly different in value and have no additional features. Various perfusion flow rates were examined, and hepatic function observed under identical experimental conditions was correlated to the computationally determined values of shear stress on the hepatocytes. Results suggest that 0.1 Pa is the maximum shear stress under which hepatocytes maintain their physiologic phenotype.

The effects of fluid flow inside single tissue-filled microchannels within the silicon scaffold were investigated by defining the channel cross-sectional geometries to reflect the representative geometries of void spaces within the tissue structures observed experimentally. One such characteristic flow path geometry was a cylinder of ∼100 μm diameter. Fluid dynamic forces in the reactor are not sufficient to cause flow induced deformation of the tissue, and thus the surface is assumed to be rigid with no slip between the fluid and tissue. Flow fields were studied inside a single channel, where tissue ringed the channel leaving a 100 μm diameter cylindrical void at the center of the scaffold. Under typical flow conditions, shear stresses at the walls are ∼0.07 Pa (see Fig. 16).

Computational analysis of mass transport in the model confirms that the hepatocytes receive sufficient
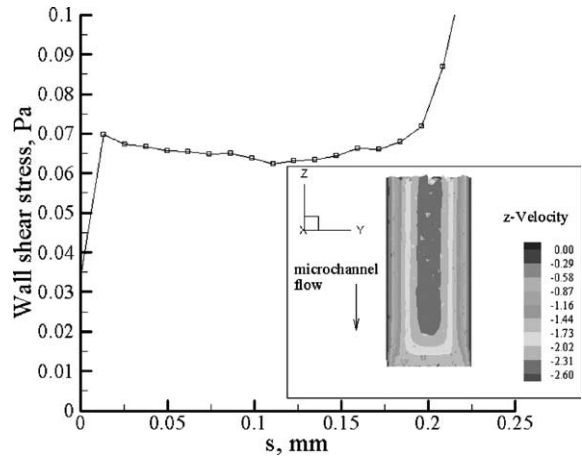
Fig. 16. Fluid dynamics in a typical tissue-filled perfusion microchannels: Wall shear stress at different positions along the tissue-filled channels ($s = 0$ represents the top of the channel). Fluid velocity in mm/s (inset).

oxygen for metabolic purposes, even under the most stringent conditions of no perfusion, i.e. in the case where all nutrient transport into the channels is via diffusion from fluid in the upper and lower chambers.

2.5.4. Summary

A 3D perfused bioreactor is presented for liver tissue culture. Computational FEM analysis of the flow and mass transport proves that the design mimics the perfusion conditions present in vivo, ensuring a physiologically relevant environment for liver tissues.

3. Concluding discussion

We have presented a few of the many examples demonstrating the critical role played by modeling and simulation in understanding fundamental biological phenomena and in the design of biological systems. Computational modeling is now routinely used, largely due to the advantages over experiments in terms of the control one can exert over the relevant parameters and the wealth of information that can be obtained. Another advantage is that the natural variability of a biological system is eliminated so that differences in behavior can be more clearly identified. The challenge, as with most modeling studies, is to create a model that is simple, yet retains the essential physical and biological attributes.

Although we have limited our examples here to problems that can be described by a continuum approach, other computational methods that allow explicit recognition of molecular-scale phenomena also play a crucial and rapidly expanding role in biology and physiology. With the development of new techniques, it will
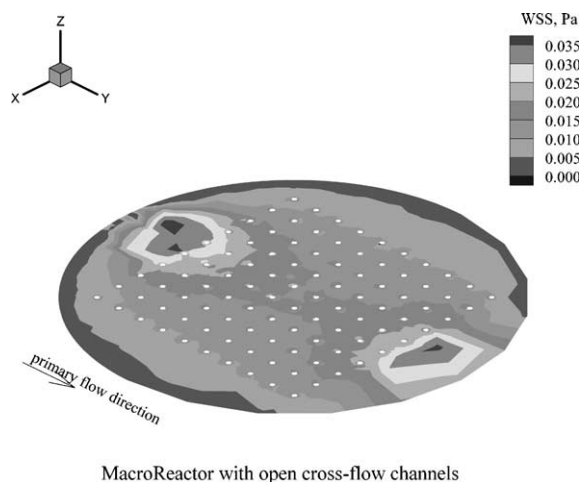

Fig. 15. Wall shear stresses (in Pa) at the chip surface in the upper chamber of the MacroReactor. Fluid enters from the left and flows out both through the right-hand channel and through the cross-flow microchannels.

become increasingly feasible to extend numerical investigations to smaller (nano)scales, e.g. the study of molecular dynamics of conformational changes in individual proteins or ion channels. More importantly, this will allow for coupled multi-scale simulations of biological phenomena over a range of time and length scales. This represents both a challenge and an opportunity. The intrinsic coupling of biological phenomena on multiple scales raises the need to understand the entire scope of a disease or biological process. For instance, to 'model' the progression of atherosclerosis we need to understand how external factors/signals influence the biological response of tissues and cells and how the consequent stimulations/deformations are mechanically transduced through cell membranes to the underlying proteins. These in turn lead to conformational changes in individual proteins that elicit biological responses reflected through the remodeling of large organs and tissues—the multi-scale cascade of biological processes works in both directions. Computational methods are hence needed that range from large-scale, whole-body cardiovascular network models down to molecular dynamics models of proteins. These will become the tools of bioengineers, biologists and physiologists as they continue to unravel the mysteries of health and disease.

References

[1] Bathe KJ. Finite element procedures. NJ: Prentice-Hall; 1996.

[2] Bathe M, Shirai A, Doerschuk CM, Kamm RD. Neutrophil transit times through pulmonary capillaries: The effects of capillary geometry and fMLP-stimulation. Biophys J 2002;83:1917–33.

[3] Bathe KJ, Zhang H, Ji S. Finite element analysis of fluid flows fully coupled with structural interactions. Comput Struct 1999;72:1–16.

[4] Berger SA, Jou LD. Flows in stenotic vessels. Ann Rev Fluid Mech 2000;32:347–84.

[5] Boulbitch AA. Strain of a biomembrane caused by a local tangential force: application to magnetic tweezer measurements. Phys Rev B 1999;59(3):3402–7.

[6] Brezzi F, Fortin M. Mixed and hybrid finite element methods. NY: Springer-Verlag; 1991.

[7] Doerschuk CM, Beyers N, Coxson HO, Wiggs B, Hogg JC. Comparison of neutrophil and capillary diameters and their relation to neutrophil sequestration in the lung. J Appl Physiol 1993;74:3040–5.

[8] Delfino A. Analysis of stress field in a model of the human carotid bifurcation. Department of Physics, Ecole Polytechnique Federale de Lausanne, Lausanne, Switzerland, 1996.

[9] Delfino A, Stergiopulos N, Moore Jr JE, Meister JJ. Residual strain effects on the stress field in a thick wall finite element model of the human carotid bifurcation. J Biomech 1997;30:777–86.

[10] Dong C, Skalak R, Sung K-LP, Schmid-Schönbein GW, Chien S. Passive deformation analysis of human leukocytes. J Biomech Eng 1988;110:27–36.

[11] Elad D, Kamm RD. Parametric evaluation of forced expiration using a numerical model. J Biomech Eng 1989; 111(3): 192–9.

[12] Evans EA. Bending elastic modulus of red blood cell membrane derived from buckling instability in micropipet aspiration tests. Biophys J 1983;43:27–30.

[13] Fung YC, Fronek K, Patitucci P. Pseudoelasticity of arteries and the choice of its mathematical expression. Am J Physiol 1979;237:H620–31.

[14] Heil M. Stokes flow in collapsible tubes—computation and experiment. J Fluid Mech 1997;353:285–312.

[15] Hogg JC, Coxson HO, Brumwell M-L, Beyers N, Doerschuk CM, MacNee W, et al. Erythrocyte and polymorphonuclear cell transit time and concentration in human pulmonary capillaries. J Appl Physiol 1994;77:1795–800.

[16] Huang H. Cellular responses to mechanical stresses applied via magnetic manipulators. PhD thesis, Medical Engineering, Massachusetts Institute of Technology, 2001.

[17] Hwang CW, Waugh RE. Energy of dissociation of lipid bilayer from the membrane skeleton of red blood cells. Biophys J 1997;72:2669–78.

[18] Ku DN, Giddens DP, Zarins CK, Glagov S. Pulsatile flow and atherosclerosis in the human carotid bifurcation. Positive correlation between plaque location and low oscillating shear stress. Arteriosclerosis 1985;5:293–302.

[19] Luo XY, Pedley TJ. Multiple solutions and flow limitation in collapsible channel flows. J Fluid Mech 2000;420:301–24.

[20] Malek AM, Alper SL, Izumo S. Hemodynamic shear stress and its role in atherosclerosis. JAMA 1999;282(21):2035–42.

[21] Powers MJ, Domansky K, Kaazempur-Mofrad MR, Kalezi A, Capitano A, Upadhyaya A, et al. A microfabricated array bioreactor for perfused 3D liver culture. Biotechnol Bioeng 2002;78(3):257–69.

[22] Reape TJ, Groot PH. Chemokines and atherosclerosis. Atherosclerosis 1999;147:213–25.

[23] Worthen GS, Schwab III B, Elson EL, Downey GP. Mechanics of stimulated neutrophils: cell stiffening induces retention in capillaries. Science 1989;245(III):183–6.

[24] Yamada S et al. Mechanics of living cells measured by laser tracking microrheology. Biophys J 2000;78:1736–47.